



OPEN

MOF-derived Co^{2+} -doped TiO_2 nanoparticles as photoanodes for dye-sensitized solar cells

R. Krishnapriya^{1,2}, C. Nizamudeen¹, B. Saini², M. Sayem Mozumder³, Rakesh K. Sharma² & A.-H. I. Mourad^{1,4,5}✉

Facile synthesis and application of nano-sized semiconductor metal oxides for optoelectronic devices have always affected fabrication challenges since it involves multi-step synthesis processes. In this regard, semiconductor oxides derived directly from metal–organic frameworks (MOFs) routes have gained a great deal of scientific interest owing to their high specific surface area, regular and tunable pore structures. Exploring the application potential of these MOF-derived semiconductor oxides systems for clean energy conversion and storage devices is currently a hot topic of research. In this study, titanium-based MIL-125(Ti) MOFs were used as a precursor to synthesize cobalt-doped TiO_2 -based dye-sensitized solar cells (DSSCs) for the first time. The thermal decomposition of the MOF precursor under an air atmosphere at 400 °C resulted in mesoporous anatase-type TiO_2 nanoparticles (NPs) of uniform morphology, large surface area with narrow pore distribution. The Co^{2+} doping in TiO_2 leads to enhanced light absorption in the visible region. When used as photoanode in DSSCs, a good power conversion efficiency (PCE) of 6.86% with good photocurrent density (J_{sc}) of 13.96 mA cm^{-2} was obtained with the lowest recombination resistance and the longest electron lifetime, which is better than the performance of the pristine TiO_2 -based photoanode.

The depletion of natural resources and environmental pollution have intensified climate change and outpaced nature's sustainability. Consequently, the advancement of sustainable clean energy technologies that are highly efficient and cost-effective is inevitable and getting innovative scientific attention^{1–4}. Alternative energy technologies such as biomass, wind, wave, geothermal, and solar energies are highly desirable to compensate for the current energy demand scenario. Amidst the above-mentioned renewable energy sources, sunlight is clean and accessible at free cost. Solar cells are ingenious devices that can effectively harness and convert sunlight directly to useful electrical energy through the photoelectric effect^{5–7}. Accordingly, solar photovoltaic (PV) technology appears very viable solution. Compared to other PV technologies, dye-sensitized solar cells (DSSCs) are prospective candidates owing to their simple solution-processable synthesis and cost-effective fabrication procedures^{8,9}.

A DSSC device mainly consists of a photoanode with a wide bandgap semiconductor (TiO_2 , ZnO , SnO_2 , etc.) layer, a photosensitizer (dye), a redox electrolyte-based on I^-/I_3^- and a Platinum-based counter electrode (CE)^{10–12}. Photoanodes are a crucial part of DSSC, and their functions include providing a high surface area to adsorb adequate dye molecules for effective light-harvesting, facilitating a suitable path for electron transport, and providing macropores for effective electrolyte diffusion. Thus, materials that possess intriguing features such as high surface area and tunable porosity, and other surface properties are prerequisites^{13–18}. To improve the light harvesting efficiency (LHE) of photoanode, strategies like the incorporation of plasmonic nanoparticles of Ag and Au as well as the use of graphene and graphdiyne materials were reported recently^{19–22}. The cell parameters, precisely, the open-circuit photovoltage (V_{oc}), short-circuit current density (J_{sc}), fill factor (FF), and the power conversion efficiency (PCE/ η), are considerably affected by the microstructures of the photoanode materials^{23,24}. Commonly used photoanode of DSSCs is TiO_2 owing to its relatively high PCE, high surface area, non-toxicity, and low cost. However, random electron transport in this material results in the recombination of electron–hole pairs leading to poor device performance.

¹Mechanical Engineering Department, College of Engineering, United Arab Emirate University, Al Ain 15551, UAE. ²Department of Chemistry, Indian Institute of Technology Jodhpur, Jodhpur 342037, Rajasthan, India. ³Department of Chemical and Petroleum Engineering, College of Engineering, United Arab Emirate University, Al Ain 15551, UAE. ⁴National Water and Energy Centre, United Arab Emirate University, Al Ain 15551, UAE. ⁵On Leave From Mechanical Design Department, Faculty of Engineering, Helwan University, Cairo, Egypt. ✉email: ahmourad@uaeu.ac.ae

Moreover, the large bandgap of TiO₂ (3.3 eV) often poses the proper excitation and injection of photoelectrons, leading to inept electron transportation and electrical conductivity. Bandgap engineering via doping with metals can moderate or reduce the optical band gap by introducing many intermediate energy levels in TiO₂ and can cause feasible electron transitions with minimum excitation energy^{25–27}. Such a doped semiconductor oxide layer demonstrated less recombination rate for the photogenerated electron and hole pairs with the advantage of many trapped states. This doping methodology is highly promising for semiconductor-based optoelectronic devices^{28–30}. Among various metals reported for doping, transition metal (TM) doped TiO₂ NCs have been ascertained as appropriate candidates for broad photoresponse in the visible light region and hence demonstrated as effective for solar energy conversion^{31–33}.

Additionally, extensive research has been devoted to improve the photoanode properties of DSSCs, in which the introduction of porous photoanodes made of various template-assisted synthesis was successfully employed^{34–38}. However, the broad applicability of these photoanodes were limited due to high fabrication cost and unfavorable possibilities for large scale production. Recently, mesoporous TiO₂ materials derived from metal–organic frameworks (MOFs) are getting much attention owing to their advantages, like high porosities and extraordinary variability in structural engineering^{39–41}. MOFs are a special class of porous materials formed of metal ions and organic linkers^{42,43}. It can be applied as efficient templates to fabricate hierarchically porous metal oxide nanostructures for DSSC electrode application. These MOF-derived metal oxides often benefit from precise morphologies, huge porosities, easy methods to dope heteroatoms, and metal nanoparticles. They can exhibit significant electrochemical properties, which are intrinsically inherited from the precursor MOF used^{39,44}. However, the application of MOF-derived TiO₂ is not well explored for photovoltaic applications.

ZIF-8 is the first MOF that was applied for DSSC applications, where its thin layer was coated on the conventional TiO₂ photoanode⁴⁵. The ZIF-8 coating could effectively inhibit the recombination loss of the modified device. Later interfacial modification of the photoanode layer was demonstrated using the ZIF-8 layer to enhance both the short-circuit current and the open-circuit voltage⁴⁶. Dou et al. presented a novel strategy for the application of MIL-125(Ti) for DSSCs. The hierarchically porous TiO₂ nanocrystals prepared directly via the calcination of highly porous MIL-125(Ti) showed the high surface area and pore size with enhanced PCE owing to the superior dye adsorption, quick electron transport, and enhanced charge collection efficiency⁴⁷. Hence to fabricate doped TiO₂ nanostructures through MOF route is a highly promising strategy as these materials can avail the advantages of both doping and also the intrinsically unique structural properties inherited from the MOFs precursors^{48,49}.

Here we report an efficient strategy to modify the photoanode of DSSCs using mesoporous cobalt doped TiO₂ of unique morphologies derived from MIL-125(Ti) for the first time. The prepared doped TiO₂ nanostructured TiO₂ exhibited a PCE as high as 6.86% with a reduced bandgap. Extended visible light absorption was observed, which facilitated more absorbed photons as charge carriers with suppressed recombination rate. This simple method to modify the photoanode resulted in enhanced J_{sc} and PCE with reduced recombination loss, demonstrate the possibility of improving the next-generation DSSC photoanode to achieve promising device performance.

Results and discussion

MIL-125(Ti) MOF was fabricated through a solvothermal process reported in previous literature⁴⁸. Figure 1a shows the powder X-ray diffraction (PXRD) patterns of MIL-125(Ti), cobalt incorporated MIL-125(Ti), and the calcined MOF derived pristine and doped TiO₂. Before the calcination process, the diffraction peaks obtained at $2\theta = 6.7^\circ, 9.5^\circ, 9.7^\circ, 11.5^\circ, \text{ and } 16.6^\circ$ respectively; which are all in good agreement with those reported earlier for MIL-125 (Ti)^{50,51}. After calcination, the samples showed crystalline peaks with the complete transformation of MOF precursor to pure metal oxide phase^{52,53}. The observed diffraction peaks of calcined samples at $25.53^\circ, 38.54^\circ, 48.10^\circ, 55.04^\circ, 68.8^\circ, \text{ and } 75.2^\circ$ were indexed to (101), (004), (200), (105), (211), and (215) cubic crystal planes of anatase TiO₂ according to the JCPDS card number 21-1272. The obtained XRD patterns of all cobalt doped samples almost coincide with that of pure anatase TiO₂ without any peaks related to rutile or to metallic cobalt or cobalt oxide, endorsing that the anatase phase is not effected upon Co doping. A slight shift of the most intense (101) peak towards the lower 2θ values was identified for all doped samples, which is ascribed to be the expansion of the TiO₂ unit cell due to the incorporation of Co²⁺. The ionic radius of Co²⁺ (Co²⁺ = 0.79 Å) is larger than that of Ti (Ti⁴⁺ = 0.745 Å) leading to an expansion TiO₂ crystal with an increase of the lattice parameters. Also, a change in FWHM of (101) peak was observed after doping, which indicating the modification in the local structure around Ti⁴⁺ after Co doping. This confirms the successful incorporation of Co in TiO₂ lattice. Apart from these, a small peak can be observed around 30.6° for the doped samples with the gradual increase in intensity (highlighted part in Fig. 1a). It is also inferred that the spectra obtained are devoid of any impurity during the solvothermal synthesis procedure. The obtained low-intensity peaks are attributed to the small size of the TiO₂ nanoparticles formed.

The incorporation of cobalt into the TiO₂ crystal lattice can influence the bandgap. This variation in bandgap after the cobalt incorporation can be clearly identified using diffuse reflectance spectroscopy, which is given in Fig. 1b. The full coverage of the UV–vis spectral range can be evident. In comparison to the pristine sample, Co²⁺ ion-doped TiO₂ samples exhibited additional peaks in the visible region (450–800) in the sub-bandgap region. Doping has a direct influence on the optical properties of TiO₂, which extended light absorption towards the visible region due to the formation of sub-bandgap states between the conduction and valence bands with oxygen vacancy sites⁵⁴. The UV–vis diffuse reflection spectrum of pristine TiO₂ is flat in the visible (400–800 nm) region. However, the reflection decreases drastically upon doping with cobalt⁵⁵. The bandgap energy is determined from diffuse reflectance spectra following the theory of P. Kubelka and F. Munk presented in 1931 (Fig. 1c)⁵⁶. Accordingly, a gradual decrease of the optical bandgap from ~ 3.3 to ~ 2.9 eV was obtained. The UV–Visible

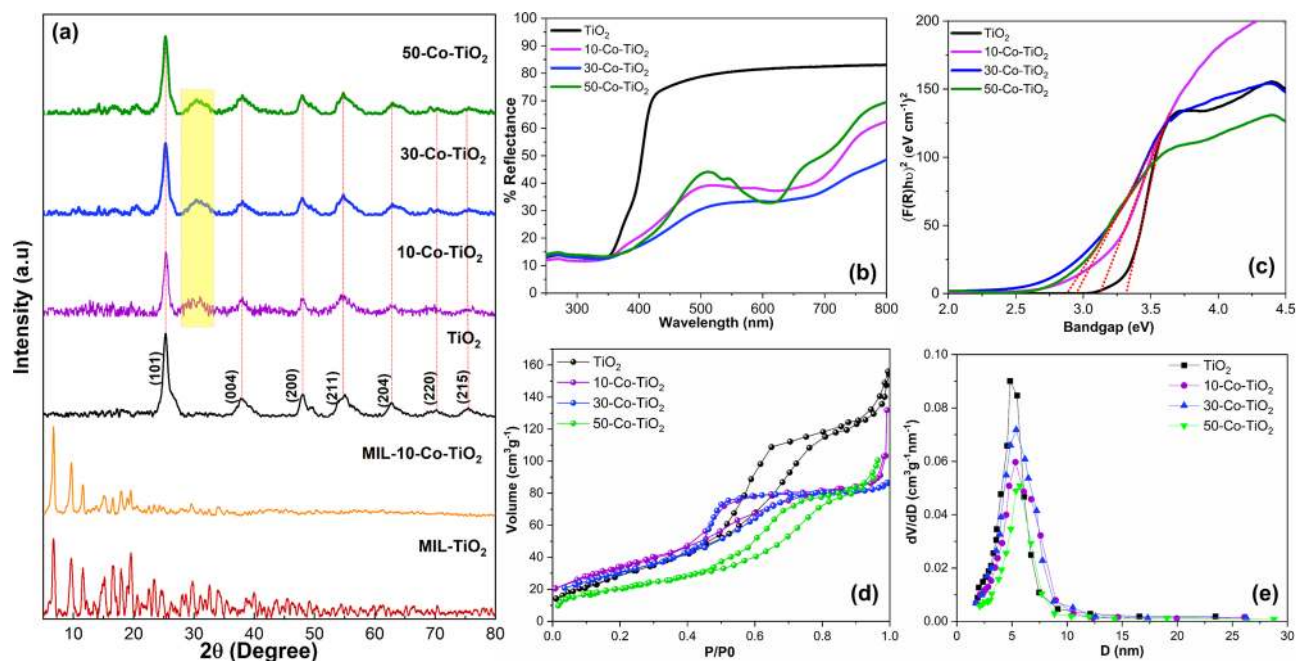


Figure 1. (a) PXRD patterns of pristine and doped MIL-125 (Ti) and the corresponding TiO₂ semiconductor oxides after thermal annealing. (b) Diffuse reflectance spectra of MOF derived TiO₂ samples and (c) its corresponding bandgap energy Kubelka–Munk plot (d) Nitrogen adsorption–desorption isotherms and (e) the corresponding BJH pore size distribution.

light response of the prepared samples was also studied by optical absorption spectroscopy of the samples in methanolic solution as in supplementary Figure S1. All of the doped samples showed much enhancement absorption compared to the pristine sample, which indicates the enhanced optical response of the samples after cobalt doping.

N₂ adsorption–desorption isotherms were measured to investigate the surface area (Fig. 1d), and pore size distribution (Fig. 1e) of all samples. The samples showed type IV isotherm curves. The BET surface area and the pore volume of undoped TiO₂ were obtained as 118 m² g^{−1} and 0.32 cm³ g^{−1}, respectively. A narrow pore size distribution around 5–6 nm was observed for TiO₂ from the BJH analysis. All the doped samples showed slightly less surface area compared to undoped samples; 10-Co-TiO₂ (92 m² g^{−1} and 0.30 cm³ g^{−1}) 30-Co-TiO₂ (90 m² g^{−1} and 0.33 cm³ g^{−1}) and 50-Co-TiO₂ (84 m² g^{−1} and 0.29 cm³ g^{−1}). Thus, the samples exhibit a relatively uniform mesoporous structure.

The morphological features of the sample before and after cobalt doping were characterized by SEM and TEM analysis. Figure 2a–d shows the SEM images of the doped and undoped samples. The undoped sample (Fig. 2a) depicted disc-like morphologies consisting of numerous nanoparticles with a diameter of 200–300 nm. Upon doping, the material showed drastic changes for both size and morphologies with very rough surfaces consisting of orderly arranged numerous nanoparticles of spherical shape with average sizes below 30 nm (Fig. 2b,c). At a higher doping concentration of cobalt, a more porous structured rough surface of the sample was perceived (Fig. 2d). The elemental identification of the sample was confirmed by EDS spectroscopy, and the spectra are given in supplementary Figure S2.

Further insights into the morphological and crystalline properties of samples were obtained from HR TEM analysis given in Fig. 3a–f. The pristine TiO₂ particle was found to be of an average size of 0.5 μm (Fig. 3a,b). The SAED pattern (Fig. 3c) shows clear, distinct rings confirming the polycrystalline nature. The obtained rings in SAED pattern were indexed (101), (200), and (201) planes of tetragonal anatase TiO₂ by calculating d-spacing. The result obtained is corroborated with the planes obtained in the XRD analysis of phase pure anatase TiO₂. For undoped TiO₂, the thickness of the particle observed was too high; as a result of this, the lattice fringes were not identified in HRTEM. However, the doped sample displayed (Fig. 3d) particle size of ~25 nm with clear lattice fringes as shown in Fig. 3e. HRTEM images displayed clear lattice fringes with d-spacing of 3.5 Å (inset figure of Fig. 3e) that matches (101) plane of tetragonal anatase phase of TiO₂, ascertaining the preferable crystal growth plane is (101), that is corroborated with the maximum intense peak obtained in XRD⁵⁷. Based on the FESEM and HR-TEM studies, the crystal growth mechanism can be explained. The formation of the precursor MOF (MIL125 (Ti)) occurred with eight TiO₆ octahedra (oh) units attached by terephthalate linkers which results in the formation of a three-dimensional (3D) microporous network. When the solvothermal reaction proceeds, the solvent ions readily enter into the microporous channel and quickly react with MIL-125 (Ti) to form TiO₂ nuclei and trigger the crystal growth process. During the crystal growth, the solvent ions prefer to adsorb on the (001) crystal faces of anatase TiO₂. Since the [001] growth direction is inhibited, other growth directions such as [100] are enhanced, resulting in nano-disk morphologies of TiO₂. A density difference occurs between MIL-125 (Ti) and TiO₂ that can readily generate cracks in the MIL-125 (Ti) crystal. Thus the MOF precursor

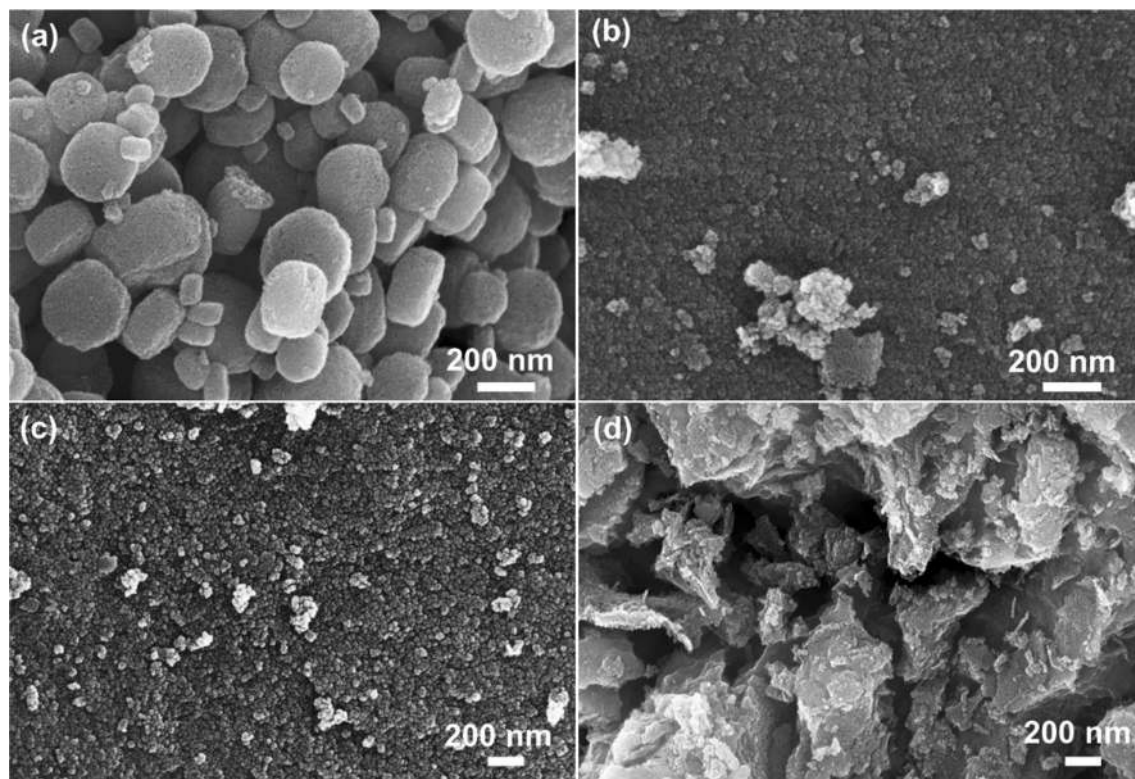


Figure 2. Morphological evolutions of MOF-derived TiO_2 samples from nanodiscs to spherical nanoparticles on doping.

breaks into pieces. The presence of Co^{2+} ions affected the crystal growth pattern and resulted in a particle-like TiO_2 NCs⁵⁸. Upon increasing the concentration of dopants the agglomeration of NCs occurs which gives more open morphological structures made of small particle like NCs.

Raman spectroscopic analysis was carried out to get more insight into the crystallinity, dopant-induced structural variations and also to understand the molecular vibration properties of all TiO_2 samples, and the spectra are shown in Fig. 4. From group theory, anatase TiO_2 has tetragonal structure and has six Raman active modes, $A_{1g} + 2B_{1g} + 3E_g$, respectively⁵⁹. E_g peak arises by O–Ti–O symmetric stretching vibration in TiO_2 , whereas B_{1g} by O–Ti–O symmetric bending vibration and A_{1g} appears due to O–Ti–O anti-symmetric bending vibration. The peaks centered at 144, 398, 518, and 641 cm^{-1} are characteristic to $E_g(1)$, B_{1g} , A_{1g} , and E_g modes, respectively. No Raman modes corresponding to the rutile phase were observed. The obtained spectra of the as-synthesized samples also showed the archetypal tetragonal form of phase pure anatase TiO_2 , which corroborates the obtained outcome from XRD. The intense $E_g(1)$ mode indicates the long-range order in the crystal. Upon doping with cobalt, the $E_g(1)$ peaks of all doped samples show a blue shift and a gradual decrease in intensity. This peak broadening, blue shifting as well as weakening of peak intensity is owing to the non-stoichiometry created owing to oxygen vacancy and phonon confinement effect due to the nanoscale size effect of the crystallites. The breakdown of long-range translational crystal symmetry occurs by the incorporation of Co^{2+} . As a result, oxygen vacancies were introduced, which results in the weakening of the Raman signals. Thus, the Raman results obtained were found to be dependable with the XRD data.

The thermal stability of the samples was studied using TGA analysis, and the resultant data are shown in supplementary Figure S3. Maximum weight loss was obtained for the MIL- TiO_2 sample before calcination, which is possibly due to the existence of residual carbon present in the sample^{60,61}. All the calcined samples (i.e., pristine and doped TiO_2) showed significantly less weight loss as well as high thermal stability. Also, it is observed that there is almost no weight loss above $250\text{ }^\circ\text{C}$, signifying that all the organic moieties were removed after the annealing process. It is noteworthy to mention that a slight weight loss $\sim 2\text{ wt.}\%$ observed below $250\text{ }^\circ\text{C}$ is due to water adsorption on the sample surface.

The chemical composition, probability of secondary phases, oxygen vacancy, and oxidation state of surface elements were revealed by X-ray photoelectron spectroscopy (XPS) of the synthesized materials. Figure 5a–f shows the XPS spectrum of TiO_2 , and 30-Co- TiO_2 , respectively. Figure 5a is the survey spectrum of both the samples, which showed the characteristic peaks of Co, Ti, and O confirms the chemical composition in materials. The status of surface elements was further examined by the high-resolution XPS spectra; Fig. 5b presents the XPS spectrum of Ti 2p with Ti $2p_{3/2}$ and Ti $2p_{1/2}$ located at 458.25 and 463.97 eV, respectively, which matches the characteristic peaks of Ti^{4+} –O bonds⁶².

From Fig. 5d of cobalt core-level spectra, peaks at binding energies of 780.64 eV of Co $2p_{3/2}$ are observed, which corresponds to the oxidation state of +2 of cobalt in TiO_2 . Another peak observed around 796.59 eV corresponds to Co $2p_{1/2}$. The spin–orbit splitting value of 15.95 eV, as well as the peak broadening, clearly supports

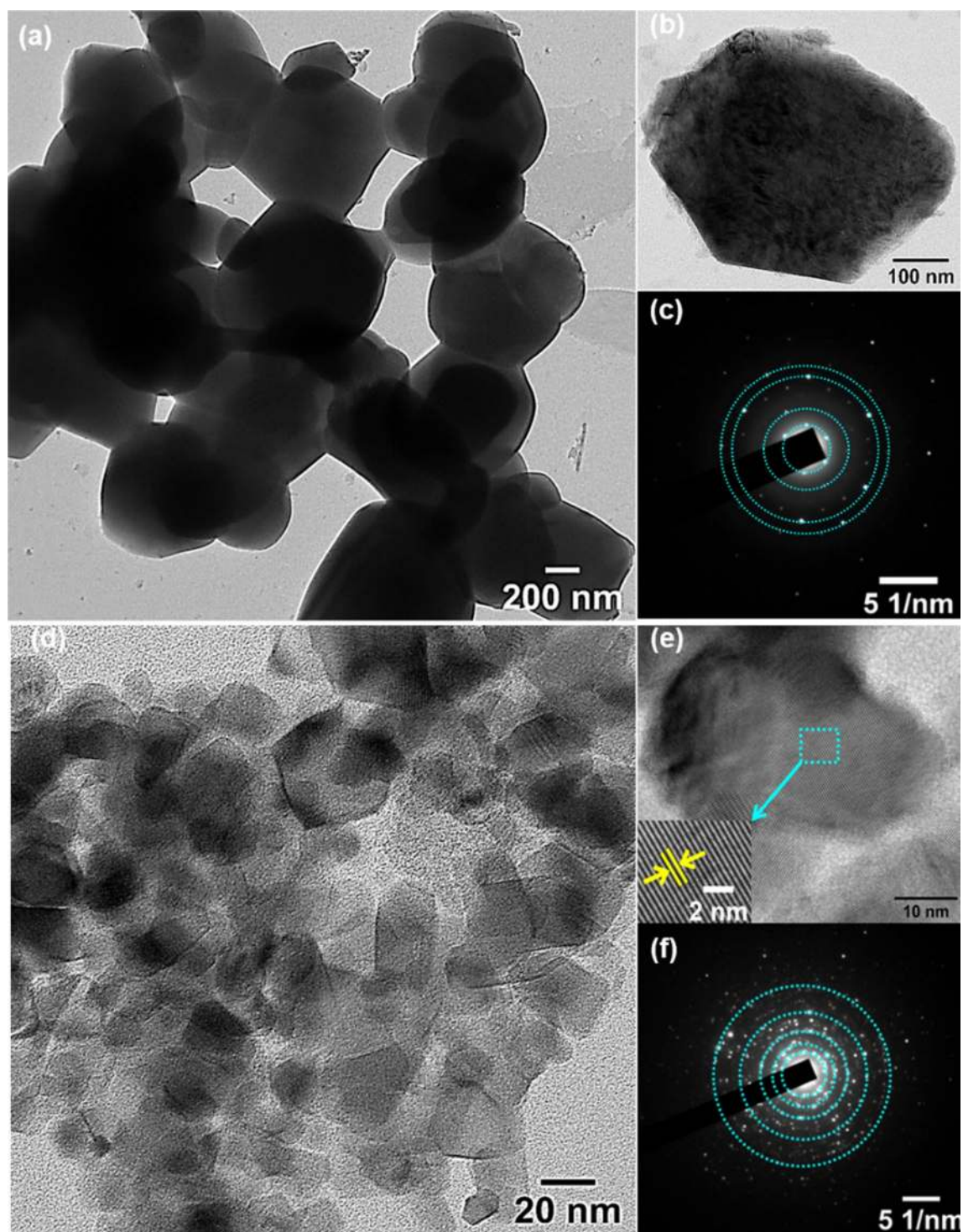


Figure 3. HR-TEM images of the MOF-derived pristine TiO_2 and cobalt doped samples.

the successful inclusion of Co^{2+} over Ti atoms in the host lattice, that generates oxygen vacancy⁶³. The presence of Ti^{3+} and Co^{2+} indicates that both samples have a definite amount of oxygen vacancies.

DSSCs fabricated with undoped as well as Co^{2+} doped samples were analyzed under simulated sunlight AM 1.5 with power 100 mW cm^{-2} . Figure 6 elucidates the J - V curves of the fabricated DSSCs. Table 1 summarizes the obtained parameters from the J - V curves, including short-circuit current density (J_{sc}), open-circuit voltage (V_{oc}), fill factor (FF), and power conversion efficiency (PCE). For the commercially available P25 titania sample, the obtained short circuit current and open-circuit voltage were $J_{sc} = 10.35 \text{ mA/cm}^2$, FF = 70.12% and $V_{oc} = 0.79 \text{ V}$ with a PCE of 5.76%.

MOF route-derived TiO_2 showed enhanced PCE of 6.06% with improved J_{sc} and V_{oc} of 10.83 mA/cm^2 and 0.799 V , respectively, however, the FF is reduced slightly to 70.05%. Upon doping with 10 mg of cobalt,

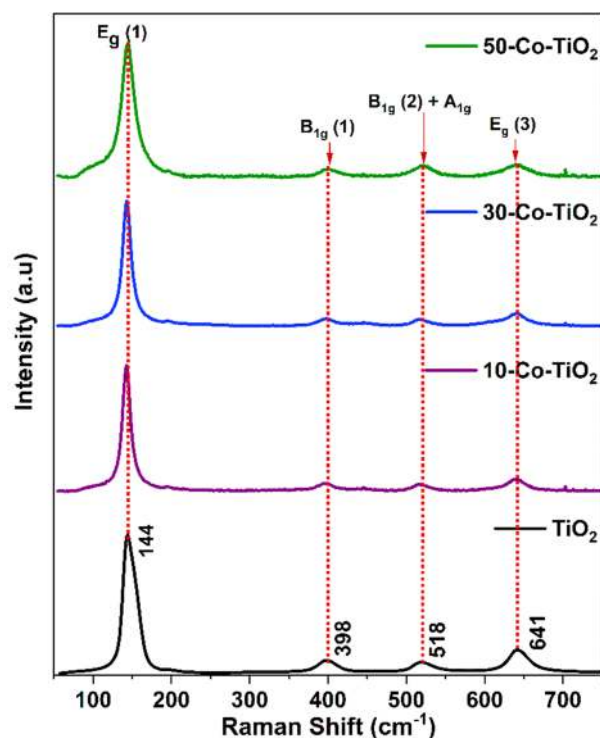


Figure 4. Room-temperature Raman spectra of pristine and doped TiO_2 .

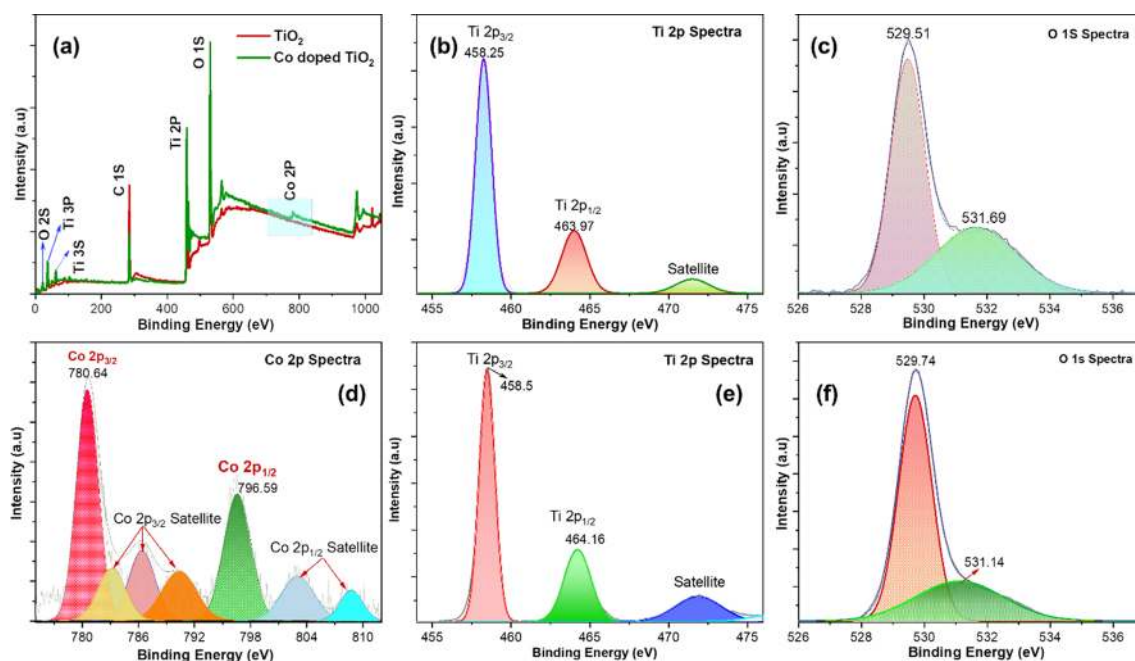


Figure 5. (a) A comparative XPS survey spectra of MOF derived TiO_2 and cobalt doped TiO_2 (b–f) Core spectra of Ti, O and Co.

an increment in J_{sc} (of 13.33 mA/cm^2) was observed while the V_{oc} (0.786) was decreased slightly. A considerable decrease in FF (61.62%) is observed. However, a net PCE of 6.46% was obtained, which showed a 12.3% improvement from the PCE data of fabricated DSSC with P25 as photoanode. When doping concentration was increased to 30 mg; PCE of 6.86% was achieved with increased $J_{sc} = 13.96 \text{ mA/cm}^2$, FF = 62.76% and slightly less $V_{oc} = 0.78 \text{ V}$. Upon further increase of cobalt to 50 mg, J_{sc} , FF and V_{oc} were decreased to 12.74 mA/cm^2 , 62.19% and 0.781 V with decreased PCE of 6.19%, but the PV performance was still greater in comparison to the pristine

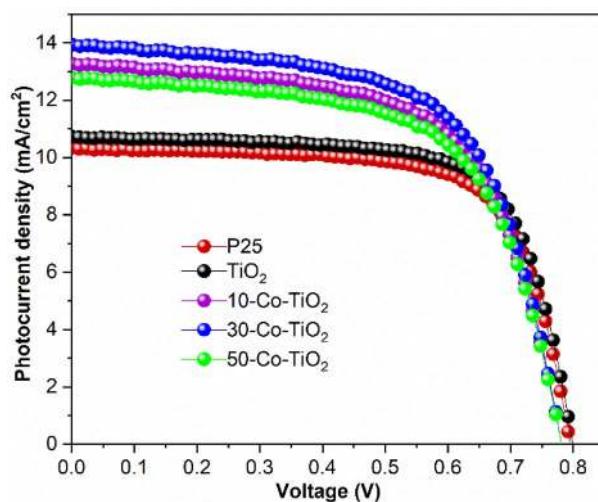


Figure 6. A comparative photocurrent density versus voltage curve (J - V) for MOF derived pristine TiO_2 and Co^{2+} ion-doped TiO_2 photoanode-based DSSCs.

Cell	J_{sc} (mA/cm^2)	V_{oc} (V)	J_{max} (mA/cm^2)	V_{max} (V)	FF (%)	PCE (%)	R_s Ω/cm^2	R_{CT} (Pt) Ω/cm^2	R_{CT} (TiO_2) Ω/cm^2
P25	10.35 ± 0.01	0.79 ± 0.01	8.91 ± 0.01	0.65 ± 0.01	70.13 ± 0.01	5.76 ± 0.01	20.36	0.86	14.72
TiO_2	10.83 ± 0.02	0.80 ± 0.01	9.53 ± 0.04	0.64 ± 0.01	70.06 ± 0.01	6.06 ± 0.02	20.79	0.45	12.97
10-Co- TiO_2	13.33 ± 0.01	0.79 ± 0.02	10.95 ± 0.01	0.59 ± 0.02	61.62 ± 0.02	6.46 ± 0.01	20.39	0.86	12.53
30-Co- TiO_2	13.96 ± 0.01	0.78 ± 0.01	11.50 ± 0.02	0.60 ± 0.01	62.76 ± 0.01	6.86 ± 0.01	20.24	0.94	11.89
50-Co- TiO_2	12.74 ± 0.03	0.78 ± 0.01	10.55 ± 0.01	0.59 ± 0.03	62.19 ± 0.01	6.19 ± 0.04	20.51	0.83	13.13

Table 1. A comparative DSSC photovoltaic performance data determined by photocurrent density–voltage (J - V) and EIS characteristic analysis of different photoanodes.

TiO_2 sample. From the obtained results, it is understood that the FF of DSSCs fabricated with doped samples were decreased compared to the reference and pristine TiO_2 based DSSCs. This can be explained as follows. The FF of a DSSC device mainly depends on the morphology and thickness of the photoanode film. Increased thickness of photoanode results in a high fill factor. However, the fill factor drops if the recombination of the charge carriers is more. Here, all the fabricated photoanodes in our study, including the reference photoanode, has the average thickness of 10–13 μm . Therefore, the difference in fill factor of DSSCs between the doped and reference photoanodes is due to the morphological difference, which can be clearly understood from the SEM and TEM characterization. Also, the BET studies showed the highly porous nature of the doped samples, which causes the excess of electrolyte diffusion into the photoanode film resulting in a high recombination rate of photogenerated electrons and subsequent reduction in FF^{64,65}. The fabricated DSSC cells were further analyzed to understand the electron lifetime and recombination characteristics with the help of the electrochemical impedance spectroscopic technique at a frequency range from 10^{-1} to 10^5 Hz with an alternative current amplitude of 10 mV. The obtained Nyquist and Bode phase plots of pure and doped samples under AM 1.5 illumination were shown in Fig. 7a,b, respectively. In the Nyquist plot (Fig. 7a), two semicircles were obtained for all the samples. In which the small semicircle in the high-frequency region corresponds to the redox as well as electron transfer reaction at the Pt counter electrode–electrolyte interface²⁴. The other large semicircle at the low-frequency region is related to the accumulation/transport of the photoinjected electrons within the photoanode film and the electron transfer across the TiO_2 /dye/electrolyte interface. This is considered as the characteristic peaks, which give a clear idea of the recombination behavior of electrons through the semiconductor oxide layer. The EIS curve is fitted using the equivalent circuit and the corresponding extracted parameters were given in Table 1. The sheet resistance (R_s) values obtained for all the devices were found to be similar and is $\sim 20 \Omega/\text{cm}^2$. The charge transfer resistance at the Pt CE interface obtained was below $1 \Omega/\text{cm}^2$ for all the devices. The DSSCs fabricated using 30-Co- TiO_2 based samples exhibited the lowest recombination resistance ($11.89 \Omega/\text{cm}^2$) compared to the reference ($14.72 \Omega/\text{cm}^2$) and undoped TiO_2 ($12.97 \Omega/\text{cm}^2$) based DSSCs. The 10-Co- TiO_2 and 50-Co- TiO_2 based DSSC devices showed slightly higher resistance, 12.53 and $13.13 \Omega/\text{cm}^2$, respectively. The result indicates the much-accelerated electron transfer in the device through reduction of charge transfer resistance resulting in an increment in J_{sc} . Figure 7b displays the Bode phase plots obtained from the impedance results. From Bode plots, the lifetime of the photo-injected electrons (τ_e) in semiconductor oxide layer can be calculated from the peak frequency (f_{max}) in the large semicircle region relate to the equation: $\tau_e = 1/2\pi f_{max}$; where f_{max} is the maximum characteristic peak

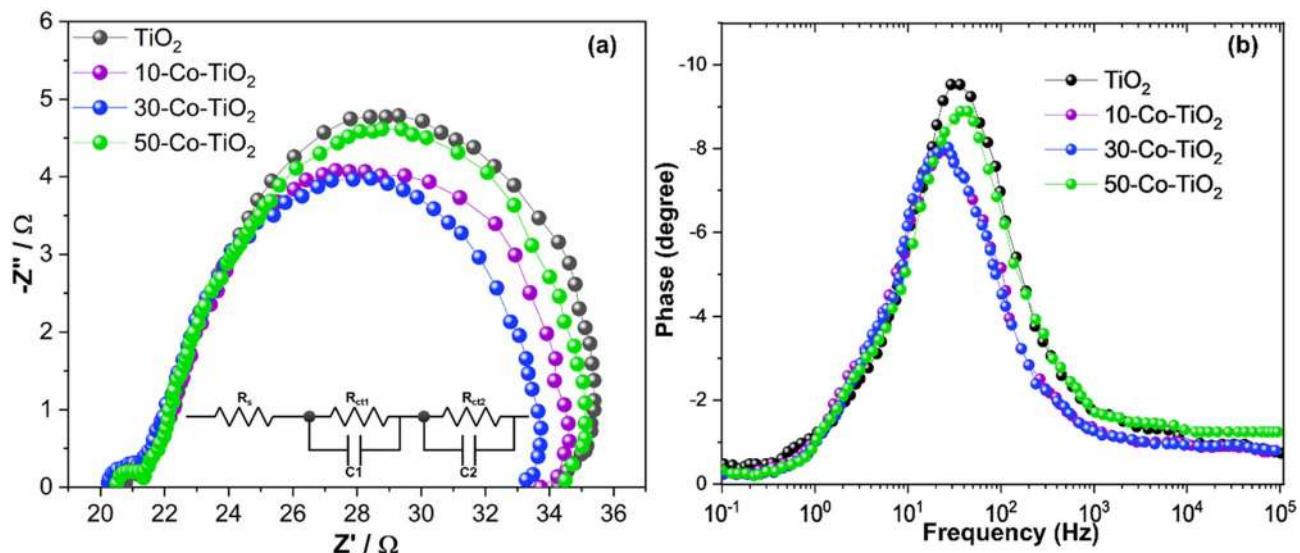


Figure 7. (a) Nyquist and (b) Bode impedance plot for TiO_2 and different Co^{2+} ion doped TiO_2 photoanode-based DSSCs. The equivalent circuit used to fit the impedance curve is inserted in (a).

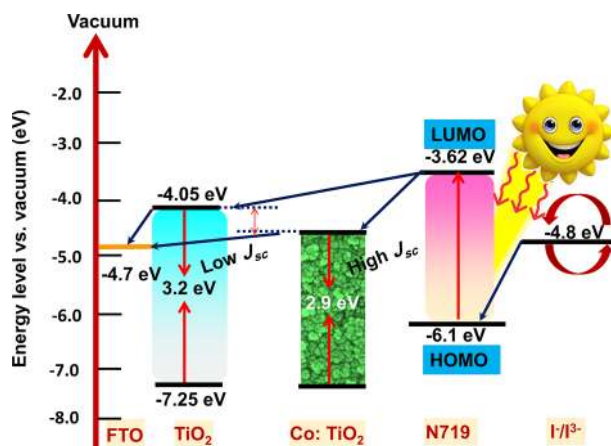


Figure 8. Schematics of possible electron transfer mechanism in MOF derived Co^{2+} ion doped TiO_2 photoanode based DSSCs.

frequency. The calculated τ values show an increased trend in a sequence of 30-Co-TiO_2 (16.1 ms) > 10-Co-TiO_2 (15.3 ms) > pure TiO_2 (6.1 ms) > 50-Co-TiO_2 (5.2 ms). In support of the Nyquist results, the 30-Co-TiO_2 based cells demonstrated the lowest recombination resistance and the longest electron lifetime, which is accountable for the uninterrupted electron transport through the oxide layer to a longer distance, leading to the enhanced PCE^{66,67}. However, at higher doping concentrations, the fabricated DSSCs revealed high recombination resistance at the semiconductor oxide/electrolyte interface with lesser τ (5.2 ms) which obstruct the cell performance by critically affecting the charge transport. On the other hand, at a lower doping concentration (10 mg of Co), the obtained τ was less (15.3 ms) as compared to 16.1 ms (for 10-Co-TiO_2). Thus the impedance spectra are directly relating to the I–V results. Also, it is evident that doping can influence the morphology and also surface chemistry of the semiconductor film. In this work, maximum PCE was achieved for the doped sample with 30 mg Co^{2+} , which was substantially ascribed to the improved surface roughness of the TiO_2 after the successful integration of cobalt ions. Moreover, the additional cobalt ions in photoanode films can prevent effective photoinduced electron–hole pairs separation by acting as recombination centers, as evident from the EIS results. The particle-like morphologies induce better interconnection that bids appropriate deployment of incident light and fast electron transport. As the doping concentration increased to 50 mg, the resulted sample shows drastic changes in morphology with lots of voids and pores, resulting in the formation of secondary impurity phases as well the incorporation of Co ions at the interstitial position. Due to this, the device shows high recombination resistance with smaller τ . Based on the above observations, the deduced electron transport over the cobalt doped TiO_2 photoanode is given in Fig. 8. Here the Co^{2+} doping in TiO_2 significantly shifted the conduction band positively, which results in an enhanced driving force of electron injection and thus increases the electron

injection efficiency from the LUMO of dye to the conduction band of TiO₂. Thus, improved light absorption and repressed charge recombination is obtained, as obvious from the UV–vis and impedance spectroscopic measurements⁶⁸. Thus, a significant improvement in *J*_{sc} was achieved. Doping could also protect the photoanode against photooxidation. Here the photon energy is effectively transferred to the Co²⁺ ions capable of quickly localizing the excitation and suppression of undesired reactions on the photoanode surface.

Conclusion

In summary, we have successfully synthesized Co²⁺ ion-doped TiO₂ nanocrystals via the MOF route. The structure and photovoltaic performance of the doped crystals were studied systematically using various characterization techniques. It was observed that the MOF-derived TiO₂ samples have more surface roughness and more conductivity. The highest PCE of 6.86% in DSSC was achieved by 30 mg Co²⁺ ion-doped TiO₂ in comparison to commercially available P25 Degussa (5.76%). The enhanced PCE was accredited to numerous factors, such as dopant-induced morphological and optical bandgap changes that resulted in improved light-harvesting efficiency with less recombination of photoinjected electrons. Better surface stability is attained after cobalt incorporation, which results in less dye aggregation on the surface with subsequent suppression in the recombination loss. The formation of several photoinduced charge carriers by charge transfer transition of Co²⁺ ions mainly contributed to the improved photocurrent, which paved the way for better PV performance. To further improve the PCE, modification of photoanode by the deposition of scattering layer and the study on its thickness is in progress.

Materials and methods

N, N-dimethyl formamide (99.8%), DMF, cobalt acetate tetrahydrate (99.99%), terephthalic acid (98%), titanium (IV) butoxide (97%), and anhydrous ethanol (98%) were purchased from Sigma Aldrich. All the reagents were used intrinsically without additional purification, and deionized water was used for all the synthesis processes. All the solvothermal reaction was carried out in a 100 mL autoclave provided by Amar Equipments Pvt. Ltd.

Characterization. The synthesized catalyst samples were analyzed by powder X-ray diffraction (PXRD) technique using a Panalytical-Empyrean X-ray diffractometer, Netherlands with Cu-K α radiation ($\lambda = 1.54 \text{ \AA}$) at 45 kV and 40 mA to scan the diffraction angles from 10° to 80°. The phase identification was carried out using standard patterns reported in the International Centre for Diffraction Data (ICDD) database. Thermogravimetric analysis (TGA) was carried out in a PerkinElmer, Simultaneous Thermal Analyzer (STA) from room temperature to 900 °C at 10 C/min under N₂ atmosphere. FESEM and HR-TEM analysis were done using Tecnai G2 F20 instrument from FEI, Netherlands operating at 200KV. For TEM study, the samples were dispersed homogeneously in isopropanol by ultrasonication and drop-casted onto a copper grid, and dried overnight before loading. Surface area and porosity measurements were analyzed using standard adsorption equipment AUTOSORB-1Q-MP-XR, Quantachrome Instruments, USA using N₂ gas with 99.995% purity. The sample was activated under a vacuum at 150 °C for 3 h followed by nitrogen adsorption–desorption isotherm measurement at 77K. The surface composition and chemical states were measured with an Omicron Nanotechnology (Oxford Instruments) X-ray photoelectron spectroscope (XPS) equipped with monochromatic Al K α radiation, and the obtained spectra were fitted by means of a Gaussian function. The peak correction was done with reference to the standard carbon 1s peak obtained at 285.07 eV. I–V analysis for the DSSC was recorded using the CHI660e from CH Instruments under one sun irradiation by PET Photo Emission Tech with SS50AAA solar simulator. Electrochemical Impedance spectroscopy (EIS) was measured by a Biologic potentiostat–galvanostat (SP-150) under an open circuit (*V*_{oc}) under illumination. The frequency ranges from 0.1 Hz to 10⁵ Hz with 10 mV alternative (AC) signal.

Synthesis: *MIL-125 synthesis.* Ti-based MOFs (i.e., MIL-125) were synthesized by the solvothermal method. To a mixture solution of terephthalic acid (3 g), anhydrous methanol (6 mL), and anhydrous DMF (54 mL), butyl titanate (4.5 mM) was added slowly with continuous stirring. The whole mixture is loaded into a 100 mL teflon-lined stainless-steel autoclave and allowed to heat to 150°C for 24 hr. After, a white suspension of MIL-125 was obtained, separated by centrifugation, and washed with methanol (3 x 50 mL). The sample is subsequently dried in a vacuum oven at 80 °C for 12 h.

TiO₂ and cobalt doped TiO₂ synthesis. The as-synthesized MIL-125 sample was annealed at 400 °C at a rate of 2°C min⁻¹ for 5 h to result in the pure titania powder stored in the sample vial for further uses. To prepare the doped TiO₂ samples, CoCl₂·6H₂O (10, 30, and 50 mg) was added to the latter reaction mixture, and the same synthesis procedure was followed. After calcination, the doped samples were obtained with light to dark green depending on the amount of cobalt precursor.

Photoanode preparation. To Prepare the DSSC photoanode, the synthesized samples (0.5g) were dispersed into 4mL ethanol by ultrasonication for 15 minutes. Then add 1.5g terpineol and 0.10g ethyl cellulose and sonicate the solution to form a homogenous viscous paste. The prepared paste was deposited on cleaned fluorine-doped tin oxide (FTO) glass substrate (transparent electrode with a typical square sheet resistance of 10 Ω /sq and overall transmittance about 85% in the visible range) by doctor blade method to get a thickness of ~13–15 μ m using 3M scotch tape into an area of 0.25 cm² (with proper masking). After drying in the air, the coated substrates were heated in a furnace (450°C for 2h). After reaching room temperature, the substrates were immersed in a 0.5 mM solution of N719 dye (Sigma-Aldrich) for 30 minutes.

Counter electrode preparation. To prepare the Pt-counter electrodes, one or two drops of 5 mM H₂PtCl₆ solution in isopropanol were drop cast onto the FTO and subsequently sintered at 400°C for 20 min. The transparent electrode obtained was used as such as the counter electrode without further heat treatment or modification.

Electrolyte preparation and assembling of DSSC. The photoanode and counter electrode were sandwiched together with surlyn film of 30 μm thickness as a spacer. Further, one or two drops of redox couple electrolyte consisting of 0.06 M 1-butyl-3-methyl imidazolium iodide, 0.03 M of iodine solution (I₂), 0.10 M guanidinium thiocyanate, 0.5 M 4-tert-butylpyridine dissolved in a mixture of acetonitrile and valeronitrile (volume ratio, 85:15), were added and introduced into the DSSC with a syringe.

Received: 17 May 2021; Accepted: 28 July 2021

Published online: 11 August 2021

References

- Linares, N., Silvestre-Albero, A. M., Serrano, E., Silvestre-Albero, J. & García-Martínez, J. Mesoporous materials for clean energy technologies. *Chem. Soc. Rev.* **43**, 7681–7717. <https://doi.org/10.1039/C3CS60435G> (2014).
- Khan, K. *et al.* Recent advances in two-dimensional materials and their nanocomposites in sustainable energy conversion applications. *Nanoscale* **11**, 21622–21678. <https://doi.org/10.1039/C9NR05919A> (2019).
- Kamat, P. V. Meeting the clean energy demand: nanostructure architectures for solar energy conversion. *J. Phys. Chem. C* **111**, 2834–2860. <https://doi.org/10.1021/jp066952u> (2007).
- Rodriguez, M. A. in *International Tables for Crystallography* 752–758.
- Nayak, P. K., Mahesh, S., Snaith, H. J. & Cahen, D. Photovoltaic solar cell technologies: Analysing the state of the art. *Nat. Rev. Mater.* **4**, 269–285. <https://doi.org/10.1038/s41578-019-0097-0> (2019).
- Hu, Z. *et al.* A critical review on semitransparent organic solar cells. *Nano Energy* **78**, 105376. <https://doi.org/10.1016/j.nanoen.2020.105376> (2020).
- Jošt, M., Kegelmann, L., Korte, L. & Albrecht, S. Monolithic perovskite tandem solar cells: A review of the present status and advanced characterization methods toward 30% efficiency. *Adv. Energy Mater.* **10**, 1904102. <https://doi.org/10.1002/aenm.201904102> (2020).
- Gong, J., Sumathy, K., Qiao, Q. & Zhou, Z. Review on dye-sensitized solar cells (DSSCs): Advanced techniques and research trends. *Renew. Sustain. Energy Rev.* **68**, 234–246. <https://doi.org/10.1016/j.rser.2016.09.097> (2017).
- Jung, H. S. & Lee, J.-K. Dye sensitized solar cells for economically viable photovoltaic systems. *J. Phys. Chem. Lett.* **4**, 1682–1693. <https://doi.org/10.1021/jz400112n> (2013).
- Listorti, A., O'Regan, B. & Durrant, J. R. Electron transfer dynamics in dye-sensitized solar cells. *Chem. Mater.* **23**, 3381–3399. <https://doi.org/10.1021/cm200651e> (2011).
- Gong, J., Liang, J. & Sumathy, K. Review on dye-sensitized solar cells (DSSCs): Fundamental concepts and novel materials. *Renew. Sustain. Energy Rev.* **16**, 5848–5860. <https://doi.org/10.1016/j.rser.2012.04.044> (2012).
- Ramya, M., Nideep, T. K., Nampoore, V. P. N. & Kailasnath, M. Solvent assisted evolution and growth mechanism of zero to three dimensional ZnO nanostructures for dye sensitized solar cell applications. *Sci. Rep.* **11**, 6159. <https://doi.org/10.1038/s41598-021-85701-9> (2021).
- Yeoh, M.-E. & Chan, K.-Y. Recent advances in photo-anode for dye-sensitized solar cells: A review. *Int. J. Energy Res.* **41**, 2446–2467. <https://doi.org/10.1002/er.3764> (2017).
- Fan, K., Yu, J. & Ho, W. Improving photoanodes to obtain highly efficient dye-sensitized solar cells: A brief review. *Mater. Horiz.* **4**, 319–344. <https://doi.org/10.1039/C6MH00511J> (2017).
- Mariotti, N. *et al.* Recent advances in eco-friendly and cost-effective materials towards sustainable dye-sensitized solar cells. *Green Chem.* **22**, 7168–7218. <https://doi.org/10.1039/D0GC01148G> (2020).
- Mozumder, M. S., Mourad, A.-H.I., Pervez, H. & Surkatti, R. Recent developments in multifunctional coatings for solar panel applications: A review. *Sol. Energy Mater. Sol. Cells* **189**, 75–102. <https://doi.org/10.1016/j.solmat.2018.09.015> (2019).
- Mozumder, M. S., Mourad, A.-H.I., Mairpady, A., Pervez, H. & Haque, M. E. Effect of TiO₂ nanofiller concentration on the mechanical, thermal and biological properties of HDPE/TiO₂ nanocomposites. *J. Mater. Eng. Perform.* **27**, 2166–2181. <https://doi.org/10.1007/s11665-018-3305-y> (2018).
- Mourad, A.-H.I., Mozumder, M. S., Mairpady, A., Pervez, H. & Kannuri, U. M. On the injection molding processing parameters of HDPE-TiO₂ nanocomposites. *Materials* **10**, 85 (2017).
- Zhang, J., Tian, J., Fan, J., Yu, J. & Ho, W. Graphdiyne: A brilliant hole accumulator for stable and efficient planar perovskite solar cells. *Small* **16**, 1907290. <https://doi.org/10.1002/smll.201907290> (2020).
- Petridis, K., Kakavelakis, G., Stylianakis, M. M. & Kymakis, E. Graphene-based inverted planar perovskite solar cells: Advancements, fundamental challenges, and prospects. *Chem. Asian J.* **13**, 240–249. <https://doi.org/10.1002/asia.201701626> (2018).
- Choudhury, B. D. *et al.* A photoanode with hierarchical nanoforest TiO₂ structure and silver plasmonic nanoparticles for flexible dye sensitized solar cell. *Sci. Rep.* **11**, 7552. <https://doi.org/10.1038/s41598-021-87123-z> (2021).
- Kaur, N., Bhullar, V., Singh, D. P. & Mahajan, A. Bimetallic implanted plasmonic photoanodes for TiO₂ sensitized third generation solar cells. *Sci. Rep.* **10**, 7657. <https://doi.org/10.1038/s41598-020-64653-6> (2020).
- Chen, H.-Y., Kuang, D.-B. & Su, C.-Y. Hierarchically micro/nanostructured photoanode materials for dye-sensitized solar cells. *J. Mater. Chem.* **22**, 15475–15489. <https://doi.org/10.1039/C2JM32402D> (2012).
- Krishnapriya, R., Praneetha, S. & Vadivel Murugan, A. Energy-efficient, microwave-assisted hydro/solvothermal synthesis of hierarchical flowers and rice grain-like ZnO nanocrystals as photoanodes for high performance dye-sensitized solar cells. *Cryst. EngComm* **17**, 8353–8367. <https://doi.org/10.1039/C5CE01438G> (2015).
- Dubey, R. S., Jadkar, S. R. & Bhorde, A. B. Synthesis and characterization of various doped TiO₂ nanocrystals for dye-sensitized solar cells. *ACS Omega* **6**, 3470–3482. <https://doi.org/10.1021/acsomega.0c01614> (2021).
- Day, J., Senthilarasu, S. & Mallick, T. K. Improving spectral modification for applications in solar cells: a review. *Renew. Energy* **132**, 186–205. <https://doi.org/10.1016/j.renene.2018.07.101> (2019).
- Unal, F. A. *et al.* Synthesis, characterization, and application of transition metals (Ni, Zr, and Fe) doped TiO₂ photoelectrodes for dye-sensitized solar cells. *J. Mol. Liq.* **299**, 112177. <https://doi.org/10.1016/j.molliq.2019.112177> (2020).
- Buonsanti, R. & Milliron, D. J. Chemistry of doped colloidal nanocrystals. *Chem. Mater.* **25**, 1305–1317. <https://doi.org/10.1021/cm304104m> (2013).
- Zhang, Y. & Hao, J. Metal-ion doped luminescent thin films for optoelectronic applications. *J. Mater. Chem. C* **1**, 5607–5618. <https://doi.org/10.1039/C3TC31024H> (2013).

30. Jiang, L. *et al.* Niobium-doped (001)-dominated anatase TiO₂ nanosheets as photoelectrode for efficient dye-sensitized solar cells. *ACS Appl. Mater. Interfaces* **9**, 9576–9583. <https://doi.org/10.1021/acsami.6b14147> (2017).
31. Janisch, R., Gopal, P. & Spaldin, N. A. Transition metal-doped TiO₂ and ZnO—present status of the field. *J. Phys.: Condens. Matter* **17**, R657–R689. <https://doi.org/10.1088/0953-8984/17/27/r01> (2005).
32. Liu, S. & Su, X. The synthesis and application of doped semiconductor nanocrystals. *Anal. Methods* **5**, 4541–4548. <https://doi.org/10.1039/C3AY40411K> (2013).
33. Ünlü, B. & Özacar, M. Effect of Cu and Mn amounts doped to TiO₂ on the performance of DSSCs. *Sol. Energy* **196**, 448–456. <https://doi.org/10.1016/j.solener.2019.12.043> (2020).
34. Anta, J. A., Guillén, E. & Tena-Zaera, R. ZnO-based dye-sensitized solar cells. *J. Phys. Chem. C* **116**, 11413–11425. <https://doi.org/10.1021/jp3010025> (2012).
35. Shakeel Ahmad, M., Pandey, A. K. & Abd Rahim, N. Advancements in the development of TiO₂ photoanodes and its fabrication methods for dye sensitized solar cell (DSSC) applications. A review. *Renew. Sustain. Energy Rev.* **77**, 89–108. <https://doi.org/10.1016/j.rser.2017.03.129> (2017).
36. Wu, Y.-H. *et al.* Green fluorine-free synthesis of hollow rectangular prism-like TiO₂ mesocrystals with exposed 001 facets for high-performance dye-sensitized solar cells. *J. Phys. Chem. C* **125**, 1684–1692. <https://doi.org/10.1021/acs.jpcc.0c08572> (2021).
37. Hejazi, S. M. H., Aghazadeh Mohandesi, J. & Javanbakht, M. The effect of functionally graded porous nano structure TiO₂ photoanode on efficiency of dye sensitized solar cells. *Sol. Energy* **144**, 699–706. <https://doi.org/10.1016/j.solener.2016.11.033> (2017).
38. Al-Attafi, K., Nattestad, A., Yamauchi, Y., Dou, S. X. & Kim, J. H. Aggregated mesoporous nanoparticles for high surface area light scattering layer TiO₂ photoanodes in dye-sensitized solar cells. *Sci. Rep.* **7**, 10341. <https://doi.org/10.1038/s41598-017-09911-w> (2017).
39. Zhao, Y. *et al.* Metal organic frameworks for energy storage and conversion. *Energy Storage Mater.* **2**, 35–62. <https://doi.org/10.1016/j.ensm.2015.11.005> (2016).
40. Chueh, C.-C. *et al.* Harnessing MOF materials in photovoltaic devices: recent advances, challenges, and perspectives. *J. Mater. Chem. A* **7**, 17079–17095. <https://doi.org/10.1039/C9TA03595H> (2019).
41. Wang, L., Zhu, Y., Du, C., Ma, X. & Cao, C. Advances and challenges in metal–organic framework derived porous materials for batteries and electrocatalysis. *J. Mater. Chem. A* **8**, 24895–24919. <https://doi.org/10.1039/D0TA08311A> (2020).
42. Furukawa, H., Cordova, K. E., O’Keeffe, M. & Yaghi, O. M. The chemistry and applications of metal–organic frameworks. *Science* **341**, 1230444. <https://doi.org/10.1126/science.1230444> (2013).
43. Li, H., Eddaoudi, M., O’Keeffe, M. & Yaghi, O. M. Design and synthesis of an exceptionally stable and highly porous metal–organic framework. *Nature* **402**, 276–279. <https://doi.org/10.1038/46248> (1999).
44. Stock, N. & Biswas, S. Synthesis of metal–organic frameworks (MOFs): Routes to various MOF topologies, morphologies, and composites. *Chem. Rev.* **112**, 933–969. <https://doi.org/10.1021/cr200304e> (2012).
45. Li, Y., Pang, A., Wang, C. & Wei, M. Metal–organic frameworks: promising materials for improving the open circuit voltage of dye-sensitized solar cells. *J. Mater. Chem.* **21**, 17259–17264. <https://doi.org/10.1039/C1JM12754C> (2011).
46. Li, Y., Chen, C., Sun, X., Dou, J. & Wei, M. Metal–organic frameworks at interfaces in dye-sensitized solar cells. *Chemosuschem* **7**, 2469–2472. <https://doi.org/10.1002/cssc.201402143> (2014).
47. Dou, J., Li, Y., Xie, F., Ding, X. & Wei, M. Metal–organic framework derived hierarchical porous anatase TiO₂ as a photoanode for dye-sensitized solar cell. *Cryst. Growth Des.* **16**, 121–125. <https://doi.org/10.1021/acs.cgd.5b01003> (2016).
48. Hong, Z. *et al.* Synthesis of mesoporous Co²⁺ doped TiO₂ nanodisks derived from metal organic frameworks with improved sodium storage performance. *ACS Appl. Mater. Interfaces* **9**, 32071–32079. <https://doi.org/10.1021/acsami.7b06290> (2017).
49. Zheng, H. *et al.* Preparation and Enhanced Electrorheological Properties of Ce-Doped Porous Titanium Oxide Nanoparticles. *Ind. Eng. Chem. Res.* **60**, 1642–1655. <https://doi.org/10.1021/acs.iecr.0c04674> (2021).
50. Liu, Z. *et al.* Effective elimination of As(III) via simultaneous photocatalytic oxidation and adsorption by a bifunctional cake-like TiO₂ derived from MIL-125(Ti). *Catal. Sci. Technol.* **8**, 1936–1944. <https://doi.org/10.1039/C8CY00125A> (2018).
51. Dan-Hardi, M. *et al.* A new photoactive crystalline highly porous titanium(IV) dicarboxylate. *J. Am. Chem. Soc.* **131**, 10857–10859. <https://doi.org/10.1021/ja903726m> (2009).
52. Chi, W. S., Roh, D. K., Lee, C. S. & Kim, J. H. A shape- and morphology-controlled metal organic framework template for high-efficiency solid-state dye-sensitized solar cells. *J. Mater. Chem. A* **3**, 21599–21608. <https://doi.org/10.1039/C5TA06731F> (2015).
53. An, Y. *et al.* Photocatalytic overall water splitting over MIL-125(Ti) upon CoPi and Pt Co-catalyst deposition. *Chemistry Open* **6**, 701–705. <https://doi.org/10.1002/open.201700100> (2017).
54. Manthina, V. & Agrios, A. G. Band edge engineering of composite photoanodes for dye-sensitized solar cells. *Electrochim. Acta* **169**, 416–423. <https://doi.org/10.1016/j.electacta.2015.04.080> (2015).
55. Gole, J. L. *et al.* Study of concentration-dependent cobalt ion doping of TiO₂ and TiO₂-xNx at the nanoscale. *Nanoscale* **2**, 1134–1140. <https://doi.org/10.1039/C0NR00125B> (2010).
56. Makula, P., Pacia, M. & Macyk, W. How to correctly determine the band gap energy of modified semiconductor photocatalysts based on UV–Vis spectra. *J. Phys. Chem. Lett.* **9**, 6814–6817. <https://doi.org/10.1021/acs.jpclett.8b02892> (2018).
57. Krishnapriya, R., Praneetha, S. & Vadivel Murugan, A. Microwave-solvothermal synthesis of various TiO₂ nano-morphologies with enhanced efficiency by incorporating Ni nanoparticles in an electrolyte for dye-sensitized solar cells. *Inorg. Chem. Front.* **4**, 1665–1678 (2017).
58. Xiu, Z. *et al.* Hierarchical porous anatase TiO₂ derived from a titanium metal–organic framework as a superior anode material for lithium ion batteries. *Chem. Commun.* **51**, 12274–12277. <https://doi.org/10.1039/C5CC03381K> (2015).
59. Ohsaka, T. Temperature Dependence of the Raman Spectrum in Anatase TiO₂. *J. Phys. Soc. Jpn.* **48**, 1661–1668. <https://doi.org/10.1143/JPSJ.48.1661> (1980).
60. Mourad, A.-H. I. Thermo-mechanical characteristics of thermally aged polyethylene/polypropylene blends. *Mater. Des.* **31**, 918–929. <https://doi.org/10.1016/j.matdes.2009.07.031> (2010).
61. Mourad, A. H. I., Akkad, R. O., Soliman, A. A. & Madkour, T. M. Characterisation of thermally treated and untreated polyethylene–polypropylene blends using DSC, TGA and IR techniques. *Plast. Rubber Compos.* **38**, 265–278. <https://doi.org/10.1179/146580109X12473409436625> (2009).
62. Liu, Z. *et al.* Hierarchical porous anatase TiO₂ microspheres with high-rate and long-term cycling stability for sodium storage in ether-based electrolyte. *ACS Appl. Energy Mater.* **3**, 3619–3627. <https://doi.org/10.1021/acsae.0c00110> (2020).
63. Chanda, A., Rout, K., Vasundhara, M., Joshi, S. R. & Singh, J. Structural and magnetic study of undoped and cobalt doped TiO₂ nanoparticles. *RSC Adv.* **8**, 10939–10947. <https://doi.org/10.1039/C8RA00626A> (2018).
64. Shalan, A. E. & Rashad, M. M. Incorporation of Mn²⁺ and Co²⁺ to TiO₂ nanoparticles and the performance of dye-sensitized solar cells. *Appl. Surf. Sci.* **283**, 975–981. <https://doi.org/10.1016/j.apsusc.2013.07.055> (2013).
65. Yacoubi, B., Samet, L., Bennaceur, J., Lamouchi, A. & Chtourou, R. Properties of transition metal doped-titania electrodes: Impact on efficiency of amorphous and nanocrystalline dye-sensitized solar cells. *Mater. Sci. Semicond. Process.* **30**, 361–367. <https://doi.org/10.1016/j.mssp.2014.10.035> (2015).
66. Wang, Q., Moser, J.-E. & Grätzel, M. Electrochemical impedance spectroscopic analysis of dye-sensitized solar cells. *J. Phys. Chem. B* **109**, 14945–14953. <https://doi.org/10.1021/jp052768h> (2005).
67. Sacco, A. Electrochemical impedance spectroscopy: Fundamentals and application in dye-sensitized solar cells. *Renew. Sustain. Energy Rev.* **79**, 814–829. <https://doi.org/10.1016/j.rser.2017.05.159> (2017).

68. Krishnapriya, R., Praneetha, S., Kannan, S. & Vadivel Murugan, A. Unveiling the Co²⁺ Ion Doping-Induced Hierarchical Shape Evolution of ZnO: In Correlation with Magnetic and Photovoltaic Performance. *ACS Sustainable Chemistry & Engineering* 5, 9981–9992, doi:<https://doi.org/10.1021/acssuschemeng.7b01918> (2017).

Acknowledgements

The authors would like to thank UAE University strategic research program (#31R238) in collaboration with the University of California, Berkeley, UAE University Ph.D. research grant (#31N414) and SERB-CRG (CRG/2020/002163) for funding the research work. We also thank CASE facility at IIT Jodhpur, CIT Coimbatore, Department of Nanoscience and Technology, University of Calicut, for material characterization.

Author contributions

R.K. and C.N. contributed equally. R.K., C.N., M.S.M. and A-H.I.M. involved in conceptualization of research idea. R.K. and C.N. analysed the results and prepared the manuscript. R.K. and B.S. performed the experiments and carried out analytical characterizations. R.K.S., M.S.M. and A-H.I.M. supervised the work. All the authors were involved in scientific discussion of the research work.

Competing interests

The authors declare no competing interests.

Additional information

Supplementary Information The online version contains supplementary material available at <https://doi.org/10.1038/s41598-021-95844-4>.

Correspondence and requests for materials should be addressed to A.-H.I.M.

Reprints and permissions information is available at www.nature.com/reprints.

Publisher's note Springer Nature remains neutral with regard to jurisdictional claims in published maps and institutional affiliations.



Open Access This article is licensed under a Creative Commons Attribution 4.0 International License, which permits use, sharing, adaptation, distribution and reproduction in any medium or format, as long as you give appropriate credit to the original author(s) and the source, provide a link to the Creative Commons licence, and indicate if changes were made. The images or other third party material in this article are included in the article's Creative Commons licence, unless indicated otherwise in a credit line to the material. If material is not included in the article's Creative Commons licence and your intended use is not permitted by statutory regulation or exceeds the permitted use, you will need to obtain permission directly from the copyright holder. To view a copy of this licence, visit <http://creativecommons.org/licenses/by/4.0/>.

© The Author(s) 2021